Nonlinear Radiative Response to Patterned Global Warming due to Convection Aggregation and Nonlinear Tropical Dynamics

Heng Quan,[a,b] Bosong Zhang,[b] Chenggong Wang,[a,b] and Stephan Fueglistaler[a,b]

[a] Department of Geosciences, Princeton University, Princeton, New Jersey
[b] Program in Atmospheric and Oceanic Sciences, Princeton University, Princeton, New Jersey

ABSTRACT: Climate responses to global warming exhibit large dependence on the spatial pattern of sea surface temperature (SST) changes. A Green's function (GF) approach—predicting the global climate response to a complex SST pattern change as the linear superposition of the response to finite-area SST perturbations evaluated in isolation—has been used to systematically evaluate and understand the top of atmosphere (TOA) radiation response to patterned warming. However, in general, the linear GF approach fails for TOA radiation reconstruction under future global warming scenarios in coupled models. Here, we show that the linear superposition of global mean TOA radiation responses to large SST warming perturbations at multiple patches (the GF approach prediction) overestimates the actual response to simultaneous multipatch perturbation. This is because the linear superposition overestimates tropical large-scale convection aggregation strengthening upon localized heating that enhances longwave radiative cooling, which is further explained by the overestimation of circulation response and associated horizontal water vapor transport. The nonadditivity of TOA radiation response is caused by the nonadditivity of convection aggregation, ultimately rooted in nonlinear tropical dynamics. We also demonstrate that the prediction error of the GF approach grows with decreasing patch size (equivalently, increasing patch number). We conclude that using the GF approach to predict future climate change could overestimate longwave radiative cooling and underestimate (effective) climate sensitivity. Numerical experiments may be used to identify specific perturbation patterns where the errors are smaller than the signal. Our research also highlights that an increase in the degree of large-scale convection aggregation has a nonlinear and negative feedback for mean warming.

KEYWORDS: Tropics; Atmospheric circulation; Deep convection; Climate sensitivity; Radiation budgets; General circulation models

1. Introduction

In marked contrast to climate simulations with coupled atmosphere–ocean general circulation models (GCMs), atmospheric general circulation model (AGCM) simulations with prescribed observed sea surface temperatures (SSTs) over the historical period (late 1800s to the present) show large, multidecadal variations of apparent climate sensitivity (global average surface temperature change due to a radiative forcing equivalent to that from doubling atmospheric CO_2) (Andrews et al. 2018, 2022). The very different behavior can be attributed to the geographical structure—or "pattern"—of changes of SST over the historical record. The far-reaching consequences of this disagreement between the observational record and coupled GCMs demand rigorous analysis of this "pattern effect" (Stevens et al. 2016). Given the potentially infinite number of possible patterns, a Green's function (GF)

approach promises a computationally feasible method to better understand the effect of any geographic structure of SST changes to radiative feedbacks and climate sensitivity (Zhou et al. 2017; Dong et al. 2019; Lewis and Mauritsen 2021; Zhang et al. 2023; Alessi and Rugenstein 2023; Bloch-Johnson et al. 2024).

The premise of the GF approach is that one can predict the climate state vector $\mathbf{\Omega}$ (with components temperature, humidity, clouds, winds, etc.) change at all locations (and hence also the global average) in response to an arbitrarily structured perturbation of SST as the linear superposition of the linearized response to SST perturbations in small domains. In discrete form for a finite-sized patch at position x_0, the total change in the state vector $\Delta\mathbf{\Omega}(x_0)$ is the sum of the single-patch responses at each position x times the SST changes at this position [$\Delta SST(x)$]:

$$\Delta\mathbf{\Omega}(x_0) = \sum_x \frac{\partial\mathbf{\Omega}(x_0)}{\partial SST(x)}\Delta SST(x), \qquad (1)$$

where $\Delta SST(x)$ represents the change of SST at grid box x and the partial derivatives $\partial\mathbf{\Omega}(x_0)/\partial SST(x)$ are calculated by localized SST warming experiments in an atmosphere model with fixed SST (Barsugli and Sardeshmukh 2002; Barsugli et al. 2006). Equation (1) requires (i) that the atmosphere responds to a perturbation of SST at one location linearly (the *linearity* condition) and (ii) that the responses to local perturbations are linearly additive (the *additivity* condition).

Empirically, it has been found that the GF approach works reasonably for the reconstruction of the global mean top of atmosphere (TOA) radiative fluxes over the historical period (Zhou et al. 2017; Dong et al. 2019; Lewis and Mauritsen 2021; Zhang et al. 2023) but fails for the reconstruction of the global mean TOA radiative fluxes in simulations of future global warming (e.g., $4\times CO_2$ forcing) (Zhang et al. 2023). In light of the pressing need to better understand the pattern effect in historical simulations, substantial effort has been directed at characterizing the errors in the GF approach and to minimize the errors through constraining the perturbation field (e.g., through requiring combinations of both warming and cooling regions) and the shape, size, and magnitude of the perturbation to calculate the unit pulse response (Zhou et al. 2017; Alessi and Rugenstein 2023; Zhang et al. 2023; Bloch-Johnson et al. 2024).

Here, we provide a theoretical framework to explain in terms of physical processes why the GF approach (in the strict mathematical sense) works in some situations but fails in others. The linearity assumption was examined in Williams et al. (2023), and we focus on the validity of the additivity assumption. Much of the pattern effect over the historical period can be traced back to the SST patterns in the tropical Pacific (Gregory and Andrews 2016; Zhou et al. 2017; Dong et al. 2019; Fueglistaler 2019; Fueglistaler and Silvers 2021; Ceppi and Fueglistaler 2021), and correspondingly, we focus on SST perturbations in the tropical Pacific (from 125.5°E to 74.5°W, 22.5°N to 22.5°S). Our analysis shows that it is the nonadditivity of tropical large-scale convection aggregation to large SST warming perturbations that breaks the additivity assumption in the GF approach. Thus, convective aggregation is not only responsible for the significance of the pattern effect but also responsible for the failure of the GF approach. The mechanism discussed here explains the nonadditivity of the longwave radiation responses as a consequence of nonlinear atmospheric dynamics, complementing earlier work that focused on the frequency distribution of boundary layer inversion strength and low clouds (Ceppi and Gregory 2017; Fueglistaler 2019) and the nonlinearity of shortwave radiation responses (Williams et al. 2023).

The paper is organized as follows. Section 2 introduces the experimental design and a metric for measuring large-scale convection aggregation. Section 3 shows our main results: We first indicate that TOA radiation responses to large SST warming perturbations in two adjacent tropical Pacific patches are nonadditive and attribute this to the nonadditivity of tropical large-scale convection aggregation responses, which is further explained by the nonadditivity of tropical circulation responses to localized heating. Then, we generalize two-patch nonadditivity to multipatch nonadditivity and discuss the failure of the GF approach using +4 K patch perturbations in future global warming scenarios. Finally, section 4 summarizes the main results and conclusions and discusses the implications for efforts to improve our understanding of the pattern effect and climate sensitivity.

2. Methods

a. Numerical experiments

We use the Geophysical Fluid Dynamics Laboratory (GFDL) atmospheric general circulation model AM4 (Zhao

et al. 2018a,b) to conduct perturbation experiments forced by patchwise SST changes in the tropical Pacific, similar to the experiments of Zhang et al. (2023). AM4 uses a horizontal grid spacing of approximately 100 km and outputs data with 180 grid points in the meridional direction and 288 in the zonal direction (i.e., $1.0° \times 1.25°$ for the horizontal resolution). The SST perturbations are applied to a control simulation forced by the observed climatological (1982–2001) monthly means of SSTs and sea ice concentrations from the HADISST1 dataset (Rayner et al. 2003). The greenhouse gas concentrations and aerosol emissions correspond to the conditions of the year 2000 and are not modified in the perturbation experiments. Following Dong et al. (2019), we integrate the control simulation for 45 years with the last 40-yr output used to compute the model's mean state. The perturbation experiments are run for 45 years, branched from the fourth year of the control run (i.e., all perturbation experiments have the same initial conditions). As for the control run, the first 5 years of the integration are discarded to allow atmospheric equilibration to the perturbation, and the climatological average of the perturbation simulations is calculated from the remaining 40 years.

Figure 1a shows the climatological mean SSTs and the 24 patches ($15° \times 20°$ each) used for the SST perturbations. The patch positions are deliberately not aligned with the underlying SST pattern: if the atmosphere satisfies the conditions for a GF approach, the sizes, shapes, and locations of the patches are not relevant other than that they constrain the set of patterns that can be represented. Uniform (within a patch) +4 K or +1 K SST perturbations are applied for simplicity.

In addition to the perturbation experiments with perpetual year 2000 conditions, we also analyze an AM4 simulation with time-varying SSTs as lower boundary conditions obtained from a coupled atmosphere–ocean general circulation model simulation of an abrupt quadrupling of atmospheric CO_2 (labeled $4\times CO_2$ experiment) using the GFDL CM4 model integrated for 150 years (Zhang et al. 2023). The longwave radiative feedback is calculated using a linear regression of the OLR as function of the global mean surface temperature. The slope of the linear regression gives an estimate of the (all sky) longwave feedback $\lambda_{ref} \approx -1.6$ W m^{-2} K^{-1}. The corresponding values for clear sky OLR and cloud radiative effect are -1.85 and 0.25 W m^{-2} K^{-1}, respectively.

b. The Gini index: A metric for large-scale convection aggregation

Following Zhang and Fueglistaler (2019), we use the Gini index, an index for inequality frequently used in economics to quantify unevenness of income and wealth, of tropical precipitation as a single-value measurement for the spatial unevenness of tropical deep convection aggregation (more clustered precipitation means more aggregated convection) (Pendergrass and Knutti 2018). The Gini index has been used to study the temporal distribution of precipitation (Rajah et al. 2014). Precipitation between 30°S and 30°N is sorted in ascending order and accumulated against the cumulative area. As illustrated in Fig. 2a, the Gini index is proportional to the shading area
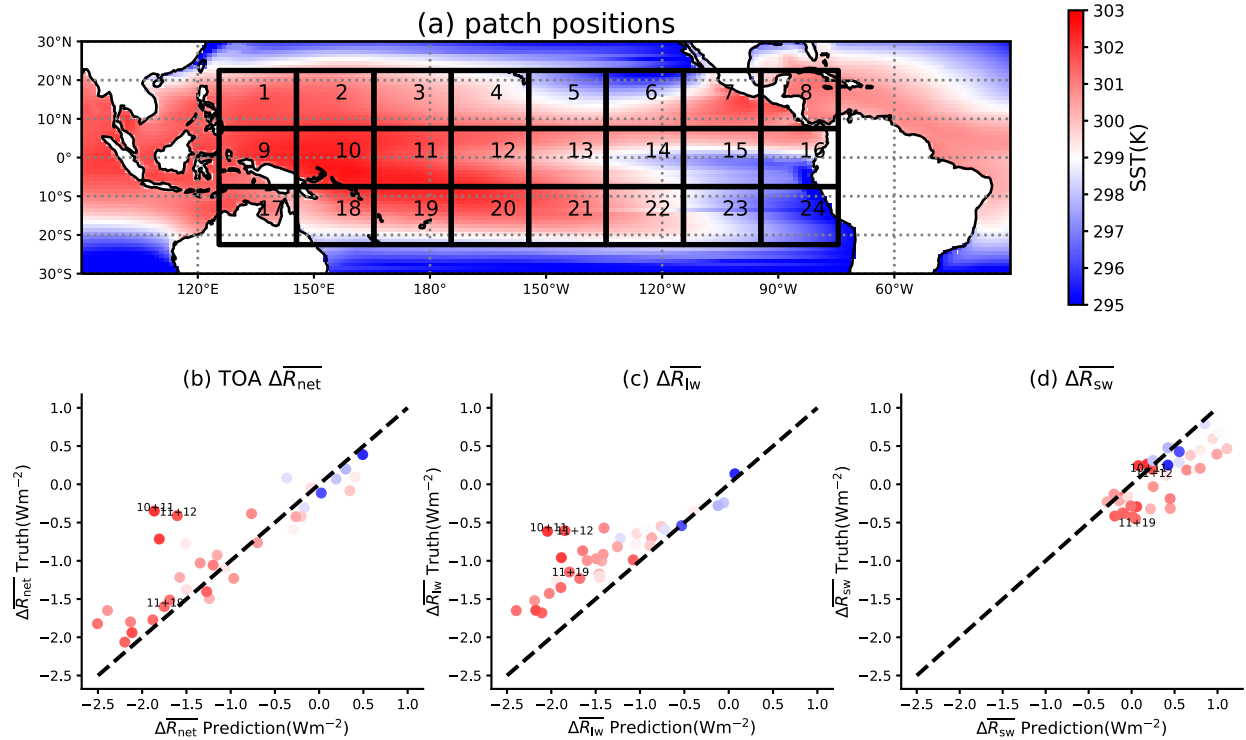
FIG. 1. (a) Climatological annual mean SST (colored contours) of the control simulation and the patches used for the +4 K experiments. (b) Change in global mean TOA net radiation $\Delta\overline{R_{net}}$ (sign convention is incoming minus outgoing radiation) following the SST perturbation in two adjacent patches (truth, y axis) and the prediction based on the linear superposition of the responses to the perturbations in two patches individually (prediction, x axis). (c) As in (b), but for the change in TOA longwave radiation $\Delta\overline{R_{lw}}$. (d) As in (b), but for the change in TOA shortwave radiation $\Delta\overline{R_{sw}}$. Colors in (b)–(d) indicate the average SST of two perturbed patches, and colors correspond to the color bar in (a).

between the $y = x$ line and the cumulative precipitation fraction (y axis) as a function of (on the x axis) cumulative area fraction (the blue line, also called the Lorenz curve). The Gini index ranges from 0 (completely uniform deep convection) to 100 (all deep convection is located in one model grid cell). Thus, an increase in the Gini index in a perturbation experiment indicates an increase in the aggregation of deep convection and vice versa for a decrease in the Gini index.

3. Results

To test the validity of the additivity assumption in the GF approach, we calculate (i) a control run climate state based on the climatological mean annual cycle of SST, (ii) the climate states following perturbations of SST in each patch individually by uniform +4 and +1 K, and (iii) the climate states following the perturbations of SST for a selected set of multiple patches. As expected, the model simulations show that for very small perturbations, the responses are approximately additive, while for perturbations of similar order as the range of tropical SST in each month (order several Kelvin), the additivity assumption of the GF approach fails. For clarity regarding the process leading to the failure of the GF approach, we show the results of +4 K experiments (nonadditive) in the

main text and discuss the +1 K results (approximately additive) in the supporting information.

a. Nonadditivity of the TOA radiative flux responses to localized SST perturbations

We start from the simplest case, i.e., testing the additivity of TOA radiation responses to localized warming perturbations in two adjacent tropical Pacific patches among the 24 patches in Fig. 1a. Figure 1b shows the actual global mean TOA net radiative flux response $\Delta\overline{R_{net}}$ (with Δ referring to perturbed minus base simulation) to simultaneous two-patch perturbation (labeled "truth"), against the predicted change based on the linear superposition of two individual responses (labeled "prediction"), for 37 pairs of adjacent patches. Generally, and consistent with theoretical intuition based on the correlation between warm SST and deep convection (Zhang 1993; Sobel et al. 2002; Fueglistaler 2019), the magnitude of the response is larger for perturbations in patches with higher SST due to nonlocal impacts (Zhou et al. 2017; Dong et al. 2019). Furthermore, Fig. 1b shows that in most cases, the GF predictions overestimate the true responses to the two-patch SST perturbations, especially for two adjacent warm and convective patches where nonlocal responses are strong.

Figures 1c and 1d decompose the global mean TOA net radiative flux $\Delta\overline{R_{net}}$ into the longwave flux $\Delta\overline{R_{lw}}$ [the negative of
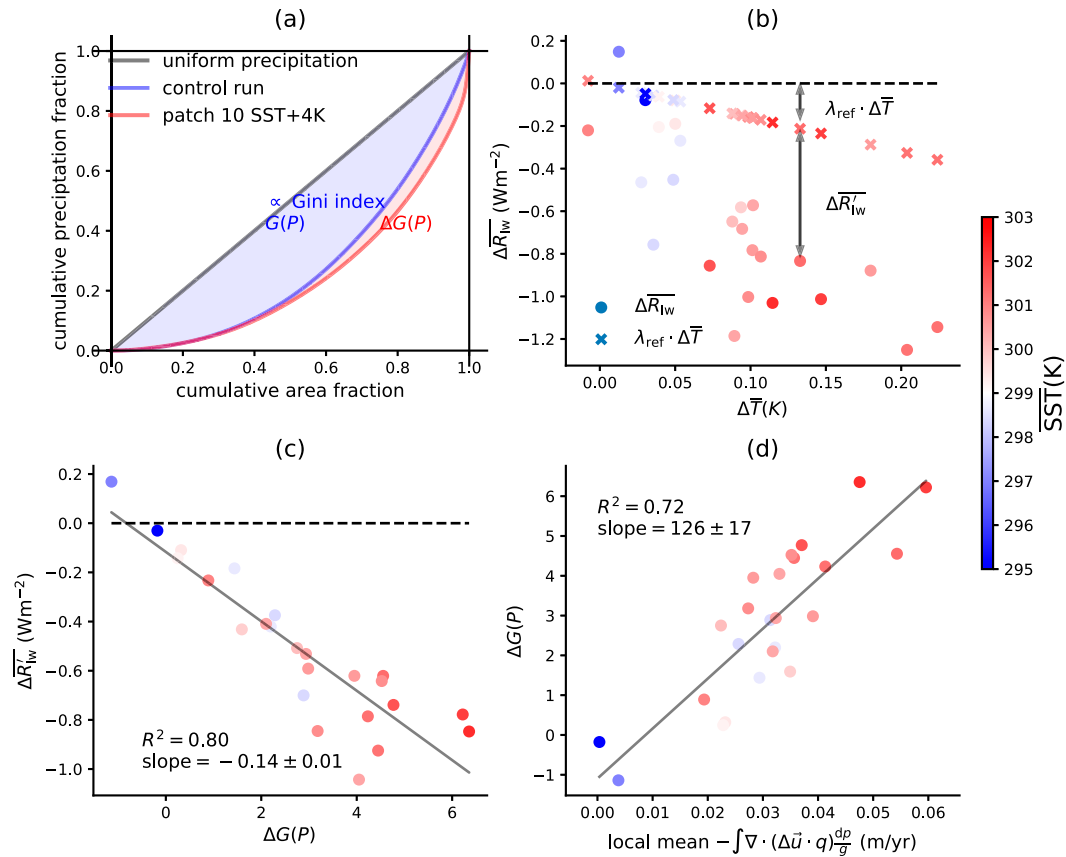
FIG. 2. (a) Schematic of tropical (30°N–30°S) precipitation Gini index (see section 2), a measure for convection aggregation strength. Lorenz curve and Gini index (blue shaded area) of the base simulation; red: example of the change in the Gini index following an increase in SST in a specific patch. (b) Relation between global mean surface temperature change (x axis) and global mean TOA longwave radiation change (y axis) between a single-patch +4 K warming experiment and the base simulation. Each filled circle corresponds to a warming of one of the patches shown in Fig. 1a. Also shown ("x" symbols) are the corresponding predicted changes in TOA longwave radiation based on the experiment's change in mean surface temperature multiplied with the longwave feedback parameter $\lambda_{\text{ref}} \approx -1.6 \text{ W m}^{-2} \text{ K}^{-1}$ calculated from a 4×CO₂ experiment (see section 2). The difference between expected change based on the reference λ_{ref} and the experiment's true change is denoted as $\Delta \overline{R'_{\text{lw}}}$, shown for one specific simulation. (c) That difference not explained by the mean surface warming $\Delta \overline{R'_{\text{lw}}}$ (y axis) is highly correlated with the change in rainfall Gini index (x axis). (d) The change in the rainfall Gini index (y axis) is highly correlated with the change in area-normalized local (i.e., perturbed patch) mean circulation-induced WVP flux convergence. Colors refer to the mean SST in the perturbed patch (color bar same to Fig. 1).

outgoing longwave radiation (OLR)] and the shortwave flux $\Delta \overline{R_{\text{sw}}}$ (incoming minus outgoing):

$$\Delta \overline{R_{\text{net}}} = \Delta \overline{R_{\text{lw}}} + \Delta \overline{R_{\text{sw}}}. \quad (2)$$

Comparison of the longwave and shortwave components shows that their respective errors are of similar magnitude but have opposite sign such that the magnitude of the error in their sum $\Delta \overline{R_{\text{net}}}$ is substantially smaller than in any term individually. Of concern here is that in almost all cases, the GF prediction substantially overestimates the magnitude of the true response in both longwave and shortwave components and that the fact that the errors cancel to some extent masks the failure of the Green's function approach when looking at $\Delta \overline{R_{\text{net}}}$ only. Dong et al. (2019) showed that the TOA radiation

responses to SST increases in two distant patches (one in the western Pacific and the other in the eastern Pacific) are additive, but Fig. 1 shows that this is not the case for *adjacent* patches. Also, the errors are much smaller for small SST perturbations (Fig. S1 in the online supplemental material), further discussed in section 3c. In the following, we focus on the nonadditivity of the longwave radiation response $\Delta \overline{R_{\text{lw}}}$, with the corresponding shortwave problem (results in supporting information) briefly discussed in section 4.

b. The role of large-scale convection aggregation

The failure of the GF approach using +4 K patch perturbations to predict the response of, for example, global mean longwave radiation to forcing from two adjacent tropical

Pacific patches can be traced to the failure to predict the strength of tropical large-scale convection aggregation, or equivalently the spatial unevenness of rainfall. As discussed above, we use the Gini index of precipitation to measure the strength of convection aggregation in the tropics (30°N–30°S). Figure 2a shows, as an example, the Lorenz curve for the +4 K experiment in patch 10, which is in the center of the Western Pacific warm pool. An increase in local SST increases precipitation locally and on average decreases remote precipitation (Fig. S4). Consequently, an increase of SST at the warm end of the SST distribution strengthens tropical convection aggregation (higher Gini index, as seen for patch 10), while an increase of SST at the cold end of the distribution (e.g., patches 23 and 24) has the opposite effect (Fig. S5a). Another frequently used metric of convection aggregation, the area fraction of subsidence (Bony et al. 2020), yields the same results (Fig. S5b).

To compare changes in TOA radiative fluxes due to a set of different SST perturbations, we must account for the fact that the experiments only control SST but not land surface temperatures, and a unit forcing of SST (e.g., uniform +4 K over a unit area) may correspond to different changes in global mean surface temperature $\Delta\overline{T}$. Focusing on the longwave radiation component $\Delta\overline{R_{\text{lw}}}$, Fig. 2b shows $\Delta\overline{R_{\text{lw}}}$ as a function of $\Delta\overline{T}$ for each single patch +4 K simulation. The longwave feedback parameter $\lambda := \Delta\overline{R_{\text{lw}}}/\Delta\overline{T}$ is different for each experiment and more negative for patches in the western Pacific warm pool [consistent with Fig. 5 in Dong et al. (2019)]. We can express the effective longwave radiation response $\Delta\overline{R_{\text{lw}}}$ as the sum of $\Delta\overline{T}$ times the *reference* feedback parameter $\lambda_{\text{ref}} \approx -1.6\,\text{W m}^{-2}\,\text{K}^{-1}$, i.e., all-sky longwave radiation feedback in a AM4 $4\times CO_2$ experiment (see section 2) and the experiment-specific departure from the canonical $4\times CO_2$ experiment $\Delta\overline{R_{\text{lw}}'}$:

$$\Delta\overline{R_{\text{lw}}} = \lambda_{\text{ref}}\Delta\overline{T} + \Delta\overline{R_{\text{lw}}'}, \qquad (3)$$

where $\lambda_{\text{ref}}\Delta\overline{T}$ represents the global mean TOA longwave radiation response we would have if surface warming had the same spatial pattern as in the $4\times CO_2$ experiment and $\Delta\overline{R_{\text{lw}}'}$ quantifies pattern effect. Figure 2b shows that the magnitude of the effective response $\Delta\overline{R_{\text{lw}}}$ of the single-patch warming experiments (filled circles) is substantially, and systematically, larger than what one would expect ("x" symbol) based on the reference feedback parameter λ_{ref}, implying the difference in $\Delta\overline{R_{\text{lw}}}$ when perturbing different patches is due to pattern effect instead of different $\Delta\overline{T}$ responses. Figure 2c shows that the discrepancy between expectation and experiment $\Delta\overline{R_{\text{lw}}'}$ can be understood from the experiment's change in the rainfall Gini index: The more the rainfall Gini index $G(P)$ changes in an experiment, the larger the discrepancy in $\Delta\overline{R_{\text{lw}}'}$.

Consistent with the previous work (Bony et al. 2016, 2020; Becker and Wing 2020; Wing et al. 2020; Zhang et al. 2021), our results show that tropical convection aggregation strengthening upon localized heating is associated with global mean midtropospheric drying (Fig. S5c) and global mean high cloud cover reduction (Fig. S5d; see also Radley and Fueglistaler 2014). By contrast, the relatively uniform warming forced by

TABLE 1. Tropical precipitation Gini index, global midtropospheric relative humidity (MTH, 700–300 hPa average), and high cloud coverage (HCC) for a control simulation, a $4\times CO_2$ global warming simulation, and the GF approach prediction (using +4 K patch warming perturbations) for the $4\times CO_2$ simulation based on the SST changes of the $4\times CO_2$ simulation. Data from Zhang et al. (2023).

	AM4 control	AM4 $4\times CO_2$	GF reconstruct
Tropical $G(P)$	43.9	42.0	74.3
$\overline{\text{MTH}}$(%)	43.1	43.0	34.8
$\overline{\text{HCC}}$(%)	37.8	37.5	30.2

$4\times CO_2$ has a much weaker effect on the tropical convection aggregation strength $G(P)$ (Zhang and Fueglistaler 2019), so midtropospheric humidity and high cloud fraction remain largely unchanged in the AM4 $4\times CO_2$ simulation (Table 1). Midtropospheric drying and high cloud cover reduction both increase outgoing longwave radiation (tropical convection aggregation weakening in patch 23 or 24 has the opposite effects). A detailed case study (see Fig. S6) shows that the stronger convection aggregation induced by localized heating in the western Pacific warm pool causes stronger ascent, an increase in midtropospheric humidity, more high clouds, and reduced OLR over the western Pacific warm pool, but weaker descent, a drier midtroposphere, less high clouds, and increased OLR away from the location of the perturbation mainly in adjacent regions. The global mean responses are dominated by the nonlocal responses (Fig. S5), such that the stronger convection aggregation in the tropics increases global mean OLR (Fig. 2c).

The convection aggregation response to localized heating is caused by the redistribution of precipitation. As shown in the appendix, the precipitation change can be decomposed according to

$$\Delta P = \Delta E - \underbrace{\int \nabla \cdot (\Delta\mathbf{u}q)\frac{dp}{g}}_{\text{dynamical}} - \underbrace{\int \nabla \cdot (\mathbf{u}\Delta q)\frac{dp}{g}}_{\text{thermodynamical}}$$
$$- \underbrace{\int \nabla \cdot (\Delta\mathbf{u}\Delta q)\frac{dp}{g}}_{\text{covariance}}, \qquad (4)$$

where ΔE is the local evaporation change and the last three terms represent the response of horizontal water vapor path (WVP) flux convergence decomposed into a dynamical term $[-\int\nabla\cdot(\Delta\mathbf{u}\cdot q)dp/g]$, a thermodynamical term $[-\int\nabla\cdot(\Delta\mathbf{u}\Delta q)dp/g]$, and a covariance term $[-\int\nabla\cdot(\Delta\mathbf{u}\Delta q)dp/g]$. Both local (perturbed region) and remote (elsewhere) mean precipitation responses are dominated by the dynamical term $[-\int\nabla\cdot(\Delta\mathbf{u}\cdot q)dp/g]$ (Figs. S7 and S8), indicating that the localized SST increase affects the large-scale convection aggregation mainly through a change in the large-scale circulation and its associated horizontal water vapor transport. This is verified by the linear relation between the change in the dynamical term and the change in the precipitation Gini index (Fig. 2d).

To summarize, the radiation response to a single-patch SST warming perturbation in the tropical Pacific is mainly caused
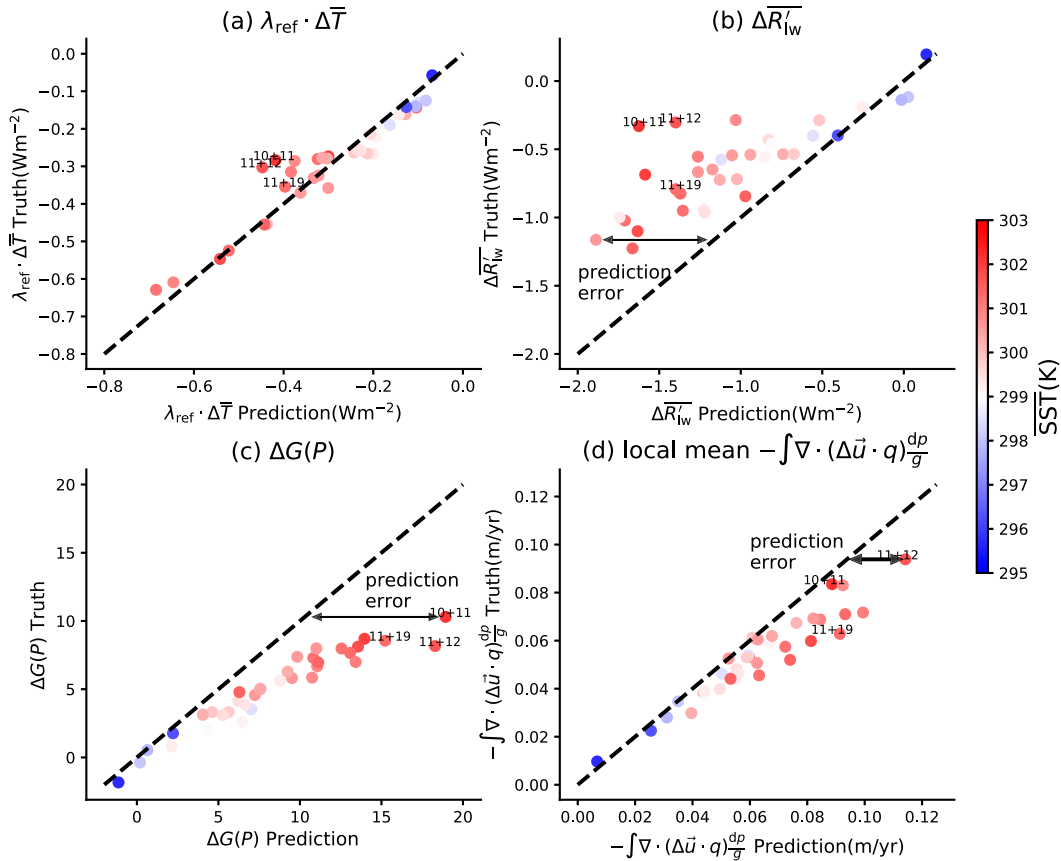
FIG. 3. Comparison of true response (y axis) following warming ($+4$ K) in two adjacent patches to the GF approach prediction (the linear sum of responses to warming in two patches individually) of (a) global average surface temperature, multiplied with λ_{ref} for comparison with (b); (b) change in TOA longwave radiation explained by convection aggregation $\Delta \overline{R'_{lw}}$; (c) tropical precipitation Gini index; (d) local (perturbed region) mean circulation-induced WVP flux convergence. Colors indicate the mean SST of the two perturbed patches (color bar as in Fig. 1).

by the response of the large-scale aggregation of convection, which in turn results from the change in large-scale circulation and associated water vapor transport.

c. Nonadditivity of convection aggregation responses to localized SST perturbations

The strength of tropical convection aggregation—expressed in terms of the Gini index of tropical rainfall—explains the much larger changes in $\Delta \overline{R'_{lw}}$ of the single-patch experiments than expected from the canonical $4 \times CO_2$ experiment. This effect is at the heart of the pattern effect and, as we will show, also leads to the failure of the GF approach using $+4$ K patch perturbations.

Figure 3 compares the results obtained from simulations with $+4$ K perturbations in two adjacent patches (truth) to the prediction based on the sum of the corresponding single-patch experiments (prediction). Figure 3a shows that the global mean surface temperature changes $\Delta \overline{T}$ are not perfectly additive, but when converted to outgoing longwave radiation by multiplication with λ_{ref}, the error in $\lambda_{ref} \cdot \Delta \overline{T}$ is small compared to the error in $\Delta \overline{R'_{lw}}$. As shown in Fig. 3b, the

failure in the linear reconstruction of $\Delta \overline{R_{lw}}$ is mostly due to the overestimate of $\Delta \overline{R'_{lw}}$.

Not surprisingly, the linear sum of the responses to individual $+4$ K perturbations in two adjacent patches overestimates local precipitation increase and remote precipitation decrease (Fig. S9). Therefore, for most warm patches, the linear sum overestimates tropical convection aggregation strengthening (Fig. 3c), and the prediction error is larger for larger $G(P)$ change. This is in turn associated with an overestimation of midtropospheric drying (Fig. S10a) and high cloud cover reduction (Fig. S10b), ultimately resulting in the overestimation of $\Delta \overline{R'_{lw}}$. As indicated by Fig. 4a, the prediction error of $\Delta \overline{R'_{lw}}$ is well explained by the prediction error of $\Delta G(P)$ [their relation is almost identical to that between $\Delta \overline{R'_{lw}}$ and $\Delta G(P)$ in Fig. 2c]. Similarly, the overestimation of midtropospheric drying (Fig. S10a) also explains the overestimation of TOA shortwave radiation $\Delta \overline{R_{sw}}$ in Fig. 1d.

Since the response of the degree of aggregation of deep convection to localized heating is mainly due to a circulation change and associated horizontal water vapor transport, we expect the prediction error of tropical rainfall Gini index $G(P)$ (Fig. 3c) to be explained by the error in the prediction
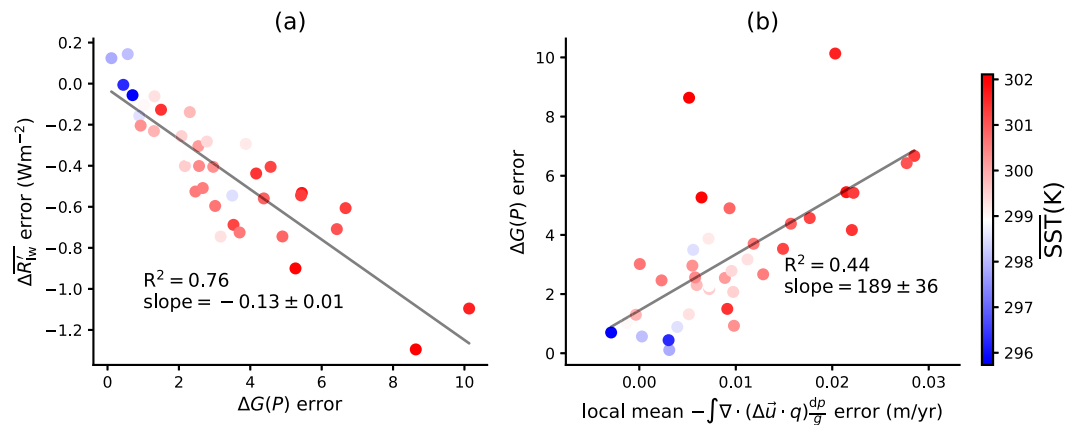
FIG. 4. Following Fig. 3, (a) the GF approach prediction error (prediction–truth) of the change in precipitation Gini index (x axis, as shown in Fig. 3c) explains the prediction error of the change in TOA longwave radiation explained by convection aggregation (y axis, $\Delta\overline{R'_{lw}}$, as shown in Fig. 3b). (b) The GF approach prediction error of the change in local mean circulation-induced WVP flux convergence (x axis, as shown in Fig. 3d) explains the prediction error of the change in precipitation Gini index. Colors indicate the mean SST of the two perturbed patches (color bar as in Fig. 1).

of the WVP convergence change $[-\int\nabla\cdot(\Delta\mathbf{u}\cdot q)dp/g]$ (Fig. 3d). Figure 4b shows that indeed the two follow closely a linear relationship (except for two outliers). While the slopes and correlations are very similar for the relation between change in the Gini index and change in $\Delta\overline{R'_{lw}}$ (Fig. 2c) and the relation between their prediction errors for the sum of two perturbed patches (Fig. 4a), the slopes and correlations differ somewhat (around one standard deviation) for the relation between Gini index and local moisture convergence (cf. slopes and correlations in Figs. 2d and 4b).

Therefore, we conclude that the TOA radiation responses to large SST warming perturbations (+4 K) in two adjacent tropical Pacific patches are not additive because of the nonadditivity of tropical large-scale convection aggregation responses (Fig. 4a), which is further explained by the nonadditivity of tropical circulation responses to localized heating (Fig. 4b). By contrast, the radiation responses to small SST warming perturbations (+1 K) are additive (Fig. S1) because convection aggregation and circulation responses are additive (Fig. S2, the +1 K counterpart of Fig. 3).

The nonadditivity of the radiation responses is ultimately rooted in the nonadditivity of the circulation responses. To better understand the latter, we provide a case study using the combination of patches 11 and 19, which requires an explanation. Figure 5 indicates that the prediction of the circulation-induced WVP flux convergence response $-\int\nabla\cdot(\Delta\mathbf{u}\cdot q)dp/g$ based on the linear sum (Fig. 5c) of the responses to the individual perturbations shows a spatial pattern similar to the actual response (Fig. 5d) but overestimates the magnitude of the local convergence (Fig. 5e). This result is consistent with previous results pointing out that while the tropical circulation response to localized heating is linearly additive in the linearized shallow water model proposed by Gill (1980), the nonlinear effects, especially nonlinear momentum transport terms, are not negligible in the free troposphere (Bao et al. 2022). As shown by Lutsko (2018), the linear theory by Gill (1980)

works for small perturbations only, while for larger perturbations, the tropical circulation response to localized heating is sublinear (Lutsko 2018). Correspondingly, the GF approach works for the (small perturbation) +1 K perturbation (see Fig. S3, the equivalent figure to Fig. 5 but with +1 K perturbations).

d. From two-patch combination to multipatch combination

The results discussed in the previous sections show that—in violation of the conditions for the validity of the GF approach—the size of the patch with perturbed SST matters. The recently published protocol for the GF Model Intercomparison Project (Bloch-Johnson et al. 2024) recognizes this problem and provides recommendations to minimize the resulting error in the GF reconstructions. The following analysis provides further insights into why and how the patch size affects the error in the GF reconstruction.

Forcing over a larger area leads to a weaker response than expected based on the sum of the responses to smaller patch forcings, eventually approaching the modest changes observed in coupled GCMs where the warming is comparatively uniform (Table 1, Zhang and Fueglistaler 2019). Consequently, we expect that the magnitude of the error in the GF prediction is a function of the size of the perturbed patch. To test this hypothesis, we carried out a set of simulations with SST forcing in eight neighboring patches (patches 1–4 and 9–12; see Fig. 6a), in which we use the GF approach to predict the response to the forcing of all eight patches based on the linear superposition of the responses to the (i) eight corresponding single-patch (smallest patch size) experiments, (ii) four corresponding two-patch (intermediate patch size) experiments, and (iii) two corresponding four-patch (large patch size) experiments.

The results shown in Figs. 6b–d confirm the hypothesis that as a rule, the smaller the patch size (equivalently, the more
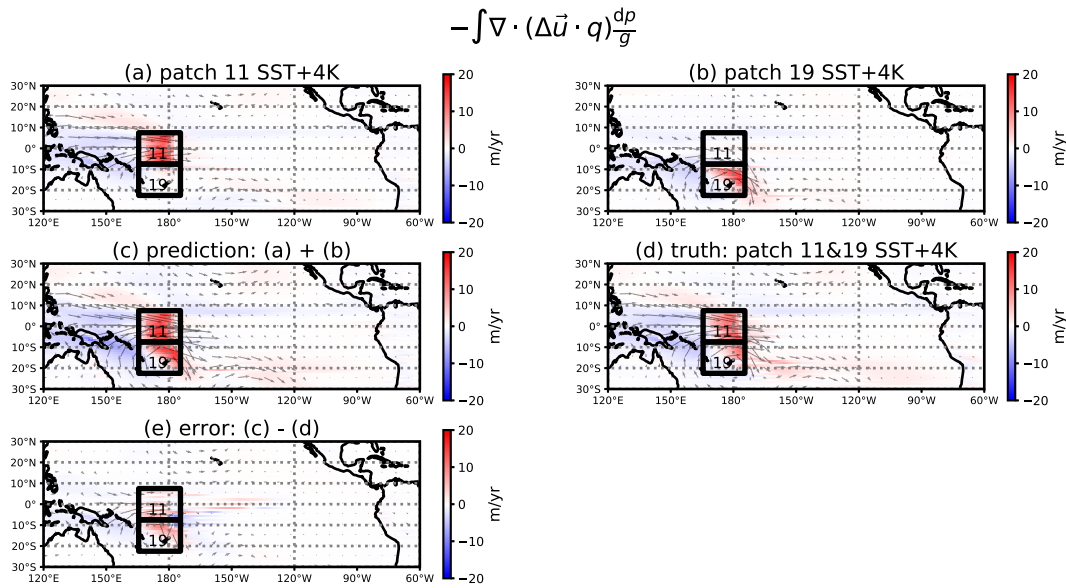
$$-\int \nabla \cdot (\Delta \vec{u} \cdot q)\frac{dp}{g}$$

FIG. 5. Nonadditivity of the circulation-induced WVP flux convergence responses $-\int \nabla \cdot (\Delta \mathbf{u} \cdot q)dp/g$ (color) to +4 K perturbations in patches 11 and 19. (a) Patch 11 + 4 K. (b) Patch 19 + 4 K. (c) Linear sum (a) + (b). (d) Patch 11&19 + 4 K. (e) Prediction error (c) − (d). Gray arrows represent the quiver plot of $\int \Delta \mathbf{u} \cdot q(dp/g)$. Linear sum overestimates local circulation-induced WVP flux convergence response, indicating tropical dynamics is nonlinear upon large perturbations.

patches) used for the GF approach, the larger the prediction error in the TOA longwave $\Delta \overline{R_{\mathrm{lw}}}$ (Fig. 6b) radiative fluxes due to the larger error in the prediction of tropical convection aggregation strength $G(P)$ (Fig. 6c), which is caused by larger error in local mean circulation-induced WVP flux convergence (Fig. 6d). The prediction error in $\Delta \overline{R_{\mathrm{lw}}}$ is larger than the error in shortwave radiation $\Delta \overline{R_{\mathrm{sw}}}$ and again dominated by its $\Delta \overline{R'_{\mathrm{lw}}}$ component (Fig. S11), which also increases when we use smaller (more) patches for the reconstruction because of the larger prediction error of midtropospheric humidity and high cloud cover (Fig. S12). Using more but smaller patches to calculate the Green's function leads to a larger error because the magnitude of the error is not linearly decreasing with decreasing patch size, such that the sum of the errors from the many smaller patches is larger than the error from the corresponding single large patch perturbation. Note that this result applies to substituting a single patch with many, smaller patches. The patch-size dependence of the error for the two-patch problem, i.e., varying the sizes of two patches in different regions, depends on the characteristics of the region. Subsidence regions with low SSTs are only weakly coupled with the surrounding atmosphere, and correspondingly in these regions, a reduction in perturbation patch size does not necessarily result in larger errors (see Fig. 3c, blue markers for "cold" regions).

4. Conclusions and outlook

The GF approach promises an elegant way to analyze and understand the climate response to forcing for any geographic structure of SST change, rather than the specific realization of the SST field of a specific simulation or observation. The results presented in this paper show that the GF approach cannot fulfill its promise in general, but may be useful for specific, experimentally determined perturbation patterns where the atmospheric response is approximately linear (Bloch-Johnson et al. 2024). On the one hand, the estimation of the local GF $\partial R/\partial$SST with a small perturbation ΔSST$\lesssim$1 K satisfies the additivity condition (Fig. S1), but the prediction is not accurate (Williams et al. 2023) for the magnitude of SST changes ($>+1$ K) of predicted future global warming. On the other hand, an evaluation of the local GF with a perturbation of the magnitude relevant for predicted future global warming (+4 K) gives an accurate global response to the local SST change, but the responses are not linearly additive. As reported by Zhang et al. (2023), using +4 K patch warming perturbation experiments to evaluate the local GF $\partial R/\partial$SST results in a substantial overestimation in the longwave radiation response compared to the true response of a 4×CO$_2$ simulation. This is because the linear superposition based on Eq. (1) overestimates the convection aggregation strength $G(P)$ and as such overestimates midtroposphere drying and high cloud cover reduction (Table 1) that enhance longwave cooling. Thus, a GF approach using +4 K patch warming perturbations is systematically biased toward overestimation of the OLR increase in response to a large SST increase, which translates to an underestimation of the climate sensitivity. The GF approach works reasonably well for the simulations over the historical period because the SST variations over that period are sufficiently small to satisfy the conditions for linear additivity. The recently published protocol for the Green's function Model Intercomparison Project (Bloch-Johnson et al. 2024) provides
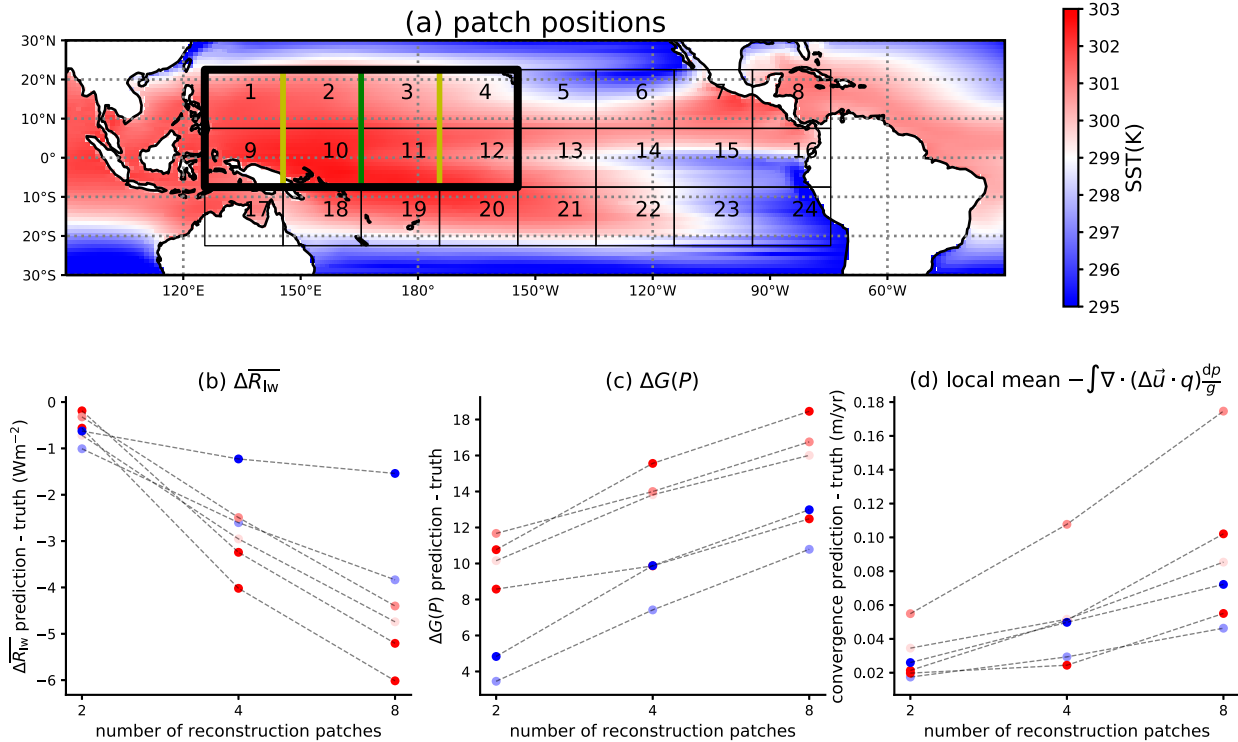
FIG. 6. Patch number dependence (or equivalently patch-size dependence) of the GF approach prediction error. (a) As in Fig. 1a, but also showing for one eight-unit patch area (bold black line), the split in four two-unit patches (yellow and green lines), and in two four-unit patches (green line). GF approach prediction errors of the changes in (b) TOA longwave radiation, (c) precipitation Gini index, and (d) local mean circulation-induced WVP flux convergence as function of the number (or equivalently inverse size) of patches used to predict the response to +4 K warming over eight-unit patches. Results shown for six different eight-unit patches; symbol colors indicate the mean SST of the eight-unit patch area (colorbar as in Fig. 3).

recommendations and instructions for experimental setups where the error in the GF approach may be within acceptable bounds.

The simulations presented here show the very strong dependency of the TOA radiative fluxes on the evenness of SSTs: the response in the TOA longwave radiation is roughly about a factor 5 larger than expected from the mean surface temperature change and the reference feedback parameter λ_{ref} (Fig. 2). It is for this reason that the "pattern effect" is important. Coupled general circulation models do not show a strong variation in the degree of aggregation, consistent with the fairly uniform changes in SSTs (Zhang et al. 2020).

The focus here on the importance of large-scale aggregation of the atmospheric circulation complements previous work highlighting the nonlinearity in the average boundary layer inversion strength to local SST perturbations arising from the nonlocal impact depending on the whether the perturbation is applied to a warm (with atmospheric deep convection) or cold (without atmospheric deep convection) part of the ocean (Williams et al. 2023). At low latitudes, the weak Coriolis force limits the magnitude of atmospheric pressure gradients in the free troposphere (Charney 1963), and correspondingly temperatures are relatively uniform and set by the conditions in the regions where deep convection couples the boundary layer and the free troposphere. A change in SSTs in

the warm regions with deep convection thus affects the boundary layer inversion strength nonlocally through a change in the free tropospheric temperature. Conversely, in a region sufficiently colder than the convective threshold, an SST change only affects the local boundary layer and only the local boundary layer inversion strength changes. Because the boundary layer inversion strength is an important factor for low clouds (Klein and Hartmann 1993; Wood and Bretherton 2006), this mechanism leads to a significant sensitivity of Earth's shortwave budget on the pattern of SST change (Ceppi and Gregory 2017; Fueglistaler 2019). The results presented here (consistent with previous studies addressing the "iris effect" (Lindzen et al. 2001; Mauritsen and Stevens 2015) show that the changes in convective aggregation following patterned warming may have an impact of comparable magnitude on the top of atmosphere longwave (and shortwave, see supplemental information, Fig. 13) radiative balance. A more uneven SST distribution corresponds to a tropical circulation with a narrower ascending branch, a reduction in high cloud cover, and a general decrease in midtropospheric humidity except for the ascending branch. Due to the nonlinear atmospheric dynamics, the aggregation effect is not linearly additive. The results presented here confirm that the Green's function approach may be used only for carefully selected problems (Bloch-Johnson et al. 2024). However, as also

evident in the results presented in this paper, the single-patch ΔSST experiments provide highly useful information about the mechanisms of tropical convective aggregation and how the degree of aggregation affects the TOA radiative fluxes and as such climate sensitivity.

Data availability statement. The model outputs are available upon request.

APPENDIX

Decomposition of Precipitation Change

We start from the water vapor path (WVP) budget equation:

$$\frac{\partial \text{WVP}}{\partial t} = -\nabla \cdot \mathbf{Q} - P + E + r, \qquad (A1)$$

where WVP is the column-integrated water vapor mass $\int q(dp/g)$ (q, p, and g are the specific humidity, pressure, and gravity) and $\mathbf{Q} = \int \mathbf{u} \cdot q(dp/g)$ is the horizontal WVP flux with $\mathbf{u} = (u, v)$ representing horizontal wind velocity. The terms P and E mean precipitation and evaporation, and r is the residual term containing other processes affecting WVP. All terms in Eq. (A1) have the dimension kilogram per square meter, and we convert it to meter per year by dividing liquid water density when presenting results below.

All analyses presented here are performed under steady state, i.e., $\partial \text{WVP}/\partial t = 0$ and Eq. (A1) reduces to

$$P = -\nabla \cdot \mathbf{Q} + E + r, \qquad (A2)$$

which states that the steady-state precipitation P is the sum of horizontal WVP flux convergence $-\nabla \cdot \mathbf{Q}$, evaporation E, and residual term r. Figure S14 verifies this equation in the control run. As expected, the WVP flux convergence $-\nabla \cdot \mathbf{Q}$ clearly shows the tropical rain belt and the residual term r are much smaller than the other three terms and can be neglected.

Our "response to localized heating" is defined as the difference between steady-state control climate and steady-state perturbed climate, so from Eq. (A2), we have

$$\Delta P = \Delta(-\nabla \cdot \mathbf{Q}) + \Delta E, \qquad (A3)$$

which decomposes the precipitation response ΔP into the response of the WVP flux convergence $\Delta(-\nabla \cdot \mathbf{Q})$ and the response of the evaporation ΔE. Figure S7 shows that the local

(remote) precipitation increase (decrease) upon localized heating is dominated by the local (remote) WVP flux convergence increase (decrease), while the response of evaporation plays a secondary role.

The response of the WVP flux convergence can be further decomposed as follows:

$$\Delta(-\nabla \cdot \mathbf{Q}) = \underbrace{-\int \nabla \cdot (\Delta \mathbf{u} q)\frac{dp}{g}}_{\text{dynamical}}$$
$$\underbrace{-\int \nabla \cdot (\mathbf{u}\Delta q)\frac{dp}{g}}_{\text{thermodynamical}} \underbrace{-\int \nabla \cdot (\Delta \mathbf{u}\Delta q)\frac{dp}{g}}_{\text{covariance}}, \qquad (A4)$$

where the three terms on the right side represent the change of WVP flux convergence due to the change of velocity/circulation (the dynamical component), specific humidity (the thermodynamical component), and their covariance. This decomposition is shown in Fig. S8, which shows that the local (remote) WVP flux convergence increase (decrease) upon a localized SST increase is dominated by $-\int \nabla \cdot (\Delta \mathbf{u} q)dp/g$. In other words, the response of WVP flux convergence upon a localized SST increase is dominated by the circulation change term.

Combining Eqs. (A3) and (A4), we have

$$\Delta P = \Delta E \underbrace{-\int \nabla \cdot (\Delta \mathbf{u} q)\frac{dp}{g}}_{\text{dynamical}} \underbrace{-\int \nabla \cdot (\mathbf{u}\Delta q)\frac{dp}{g}}_{\text{thermodynamical}}$$
$$\underbrace{-\int \nabla \cdot (\Delta \mathbf{u}\Delta q)\frac{dp}{g}}_{\text{covariance}}, \qquad (A5)$$

where both local (perturbed region) and remote (elsewhere) mean precipitation responses are dominated by $-\int \nabla \cdot (\Delta \mathbf{u} q)dp/g$.

REFERENCES

Alessi, M. J., and M. A. A. Rugenstein, 2023: Surface temperature pattern scenarios suggest higher warming rates than current projections. *Geophys. Res. Lett.*, **50**, e2023GL105795, https://doi.org/10.1029/2023GL105795.

Andrews, T., and Coauthors, 2018: Accounting for changing temperature patterns increases historical estimates of climate sensitivity. *Geophys. Res. Lett.*, **45**, 8490–8499, https://doi.org/10.1029/2018GL078887.

——, and Coauthors, 2022: On the effect of historical SST patterns on radiative feedback. *J. Geophys. Res. Atmos.*, **127**, e2022JD036675, https://doi.org/10.1029/2022JD036675.

Bao, J., V. Dixit, and S. C. Sherwood, 2022: Zonal temperature gradients in the tropical free troposphere. *J. Climate*, **35**, 7937–7948, https://doi.org/10.1175/JCLI-D-22-0145.1.

Barsugli, J. J., and P. D. Sardeshmukh, 2002: Global atmospheric sensitivity to tropical SST anomalies throughout the Indo-Pacific basin. *J. Climate*, **15**, 3427–3442, https://doi.org/10.1175/1520-0442(2002)015<3427:GASTTS>2.0.CO;2.

——, S.-I. Shin, and P. D. Sardeshmukh, 2006: Sensitivity of global warming to the pattern of tropical ocean warming.

Climate Dyn., **27**, 483–492, https://doi.org/10.1007/s00382-006-0143-7.

Becker, T., and A. A. Wing, 2020: Understanding the extreme spread in climate sensitivity within the Radiative-Convective Equilibrium Model Intercomparison Project. *J. Adv. Model. Earth Syst.*, **12**, e2020MS002165, https://doi.org/10.1029/2020MS002165.

Bloch-Johnson, J., and Coauthors, 2024: The Green's Function Model Intercomparison Project (GFMIP) protocol. *J. Adv. Model. Earth Syst.*, **16**, e2023MS003700, https://doi.org/10.1029/2023MS003700.

Bony, S., B. Stevens, D. Coppin, T. Becker, K. A. Reed, A. Voigt, and B. Medeiros, 2016: Thermodynamic control of anvil cloud amount. *Proc. Natl. Acad. Sci. USA*, **113**, 8927–8932, https://doi.org/10.1073/pnas.1601472113.

——, A. Semie, R. J. Kramer, B. Soden, A. M. Tompkins, and K. A. Emanuel, 2020: Observed modulation of the tropical radiation budget by deep convective organization and lower-tropospheric stability. *AGU Adv.*, **1**, e2019AV000155, https://doi.org/10.1029/2019AV000155.

Ceppi, P., and J. M. Gregory, 2017: Relationship of tropospheric stability to climate sensitivity and Earth's observed radiation budget. *Proc. Natl. Acad. Sci. USA*, **114**, 13 126–13 131, https://doi.org/10.1073/pnas.1714308114.

——, and S. Fueglistaler, 2021: The El Niño–Southern Oscillation pattern effect. *Geophys. Res. Lett.*, **48**, e2021GL095261, https://doi.org/10.1029/2021GL095261.

Charney, J. G., 1963: A note on large-scale motions in the tropics. *J. Atmos. Sci.*, **20**, 607–609, https://doi.org/10.1175/1520-0469(1963)020<0607:ANOLSM>2.0.CO;2.

Dong, Y., C. Proistosescu, K. C. Armour, and D. S. Battisti, 2019: Attributing historical and future evolution of radiative feedbacks to regional warming patterns using a Green's function approach: The preeminence of the western Pacific. *J. Climate*, **32**, 5471–5491, https://doi.org/10.1175/JCLI-D-18-0843.1.

Fueglistaler, S., 2019: Observational evidence for two modes of coupling between sea surface temperatures, tropospheric temperature profile, and shortwave cloud radiative effect in the tropics. *Geophys. Res. Lett.*, **46**, 9890–9898, https://doi.org/10.1029/2019GL083990.

——, and L. G. Silvers, 2021: The peculiar trajectory of global warming. *J. Geophys. Res. Atmos.*, **126**, e2020JD033629, https://doi.org/10.1029/2020JD033629.

Gill, A. E., 1980: Some simple solutions for heat-induced tropical circulation. *Quart. J. Roy. Meteor. Soc.*, **106**, 447–462, https://doi.org/10.1002/qj.49710644905.

Gregory, J. M., and T. Andrews, 2016: Variation in climate sensitivity and feedback parameters during the historical period. *Geophys. Res. Lett.*, **43**, 3911–3920, https://doi.org/10.1002/2016GL068406.

Klein, S. A., and D. L. Hartmann, 1993: The seasonal cycle of low stratiform clouds. *J. Climate*, **6**, 1587–1606, https://doi.org/10.1175/1520-0442(1993)006<1587:TSCOLS>2.0.CO;2.

Lewis, N., and T. Mauritsen, 2021: Negligible unforced historical pattern effect on climate feedback strength found in HadISST-based AMIP simulations. *J. Climate*, **34**, 39–55, https://doi.org/10.1175/JCLI-D-19-0941.1.

Lindzen, R. S., M.-D. Chou, and A. Y. Hou, 2001: Does the Earth have an adaptive infrared Iris? *Bull. Amer. Meteor. Soc.*, **82**, 417–432, https://doi.org/10.1175/1520-0477(2001)082<0417:DTEHAA>2.3.CO;2.

Lutsko, N. J., 2018: The response of an idealized atmosphere to localized tropical heating: Superrotation and the breakdown of linear theory. *J. Atmos. Sci.*, **75**, 3–20, https://doi.org/10.1175/JAS-D-17-0192.1.

Mauritsen, T., and B. Stevens, 2015: Missing iris effect as a possible cause of muted hydrological change and high climate sensitivity in models. *Nat. Geosci.*, **8**, 346–351, https://doi.org/10.1038/ngeo2414.

Pendergrass, A. G., and R. Knutti, 2018: The uneven nature of daily precipitation and its change. *Geophys. Res. Lett.*, **45**, 11 980–11 988, https://doi.org/10.1029/2018GL080298.

Radley, C., and S. Fueglistaler, 2014: The role of large-scale convective organization for tropical high cloud amount. *Geophys. Res. Lett.*, **41**, 5259–5263, https://doi.org/10.1002/2014GL060904.

Rajah, K., T. O'Leary, A. Turner, G. Petrakis, M. Leonard, and S. Westra, 2014: Changes to the temporal distribution of daily precipitation. *Geophys. Res. Lett.*, **41**, 8887–8894, https://doi.org/10.1002/2014GL062156.

Rayner, N. A., D. E. Parker, E. B. Horton, C. K. Folland, L. V. Alexander, D. P. Rowell, E. C. Kent, and A. Kaplan, 2003: Global analyses of sea surface temperature, sea ice, and night marine air temperature since the late nineteenth century. *J. Geophys. Res.*, **108**, 4407, https://doi.org/10.1029/2002JD002670.

Sobel, A. H., I. M. Held, and C. S. Bretherton, 2002: The ENSO signal in tropical tropospheric temperature. *J. Climate*, **15**, 2702–2706, https://doi.org/10.1175/1520-0442(2002)015<2702:TESITT>2.0.CO;2.

Stevens, B., S. C. Sherwood, S. Bony, and M. J. Webb, 2016: Prospects for narrowing bounds on Earth's equilibrium climate sensitivity. *Earth's Future*, **4**, 512–522, https://doi.org/10.1002/2016EF000376.

Williams, A. I., N. Jeevanjee, and J. Bloch-Johnson, 2023: Circus tents, convective thresholds, and the non-linear climate response to tropical SSTs. *Geophys. Res. Lett.*, **50**, e2022GL101499, https://doi.org/10.1029/2022GL101499.

Wing, A. A., and Coauthors, 2020: Clouds and convective self-aggregation in a multimodel ensemble of radiative-convective equilibrium simulations. *J. Adv. Model. Earth Syst.*, **12**, e2020MS002138, https://doi.org/10.1029/2020MS002138.

Wood, R., and C. S. Bretherton, 2006: On the relationship between stratiform low cloud cover and lower-tropospheric stability. *J. Climate*, **19**, 6425–6432, https://doi.org/10.1175/JCLI3988.1.

Zhang, B., B. J. Soden, G. A. Vecchi, and W. Yang, 2021: Investigating the causes and impacts of convective aggregation in a high resolution atmospheric GCM. *J. Adv. Model. Earth Syst.*, **13**, e2021MS002675, https://doi.org/10.1029/2020GL089235.

——, M. Zhao, and Z. Tan, 2023: Using a Green's function approach to diagnose the pattern effect in GFDL AM4 and CM4. *J. Climate*, **36**, 1105–1124, https://doi.org/10.1175/JCLI-D-22-0024.1.

Zhang, C., 1993: Large-scale variability of atmospheric deep convection in relation to sea surface temperature in the tropics. *J. Climate*, **6**, 1898–1913, https://doi.org/10.1175/1520-0442(1993)006<1898:LSVOAD>2.0.CO;2.

Zhang, Y., and S. Fueglistaler, 2019: Mechanism for increasing tropical rainfall unevenness with global warming. *Geophys. Res. Lett.*, **46**, 14 836–14 843, https://doi.org/10.1029/2019GL086058.

——, N. Jeevanjee, and S. Fueglistaler, 2020: Linearity of outgoing longwave radiation: From an atmospheric column to global climate models. *Geophys. Res. Lett.*, **47**, e2020GL089235, https://doi.org/10.1029/2020GL089235.

Zhao, M., and Coauthors, 2018a: The GFDL global atmosphere and land model AM4.0/LM4.0: 1. Simulation characteristics with prescribed SSTs. *J. Adv. Model. Earth Syst.*, **10**, 691–734, https://doi.org/10.1002/2017MS001208.

——, and Coauthors, 2018b: The GFDL global atmosphere and land model AM4.0/LM4.0: 2. Model description, sensitivity studies, and tuning strategies. *J. Adv. Model.*

Earth Syst., **10**, 735–769, https://doi.org/10.1002/2017MS001209.

Zhou, C., M. D. Zelinka, and S. A. Klein, 2017: Analyzing the dependence of global cloud feedback on the spatial pattern of sea surface temperature change with a Green's function approach. *J. Adv. Model. Earth Syst.*, **9**, 2174–2189, https://doi.org/10.1002/2017MS001096.